A Density Functional Theory Study of Electrochemical Nitrogen Reduction to Ammonia on the (100) Surface of Transition Metal Oxynitrides

Damilola Ologunagba, and Shyam Kattel*

Department of Physics, Florida A&M University

Tallahassee, FL 32307 USA

*Corresponding author: shyam.kattel@famu.edu

ABSTRACT

The electrochemical nitrogen (N_2) reduction reaction (ENRR) to produce ammonia (NH_3) at ambient conditions is attractive compared to the energy and carbon-intensive industrialized Haber-Bosch process. However, efficient catalysts are needed to break an N≡N bond in N_2 molecule to convert it to NH_3. Transition metal oxynitrides (TMNOs) have shown promising ENRR activities at low potentials. Here, density functional theory (DFT) calculations are performed to study the ENRR activity of TMNO(100) surfaces for TM = Co, Cr, Cu, Fe, Hf, Mn, Nb, Ni, Sc, Ta, Ti, V, Y, Zn, Zr. Our DFT calculations and microkinetic modeling results show that the ENRR proceeds at a low applied potential on the (100) surfaces of MnNO, CrNO, FeNO, CuNO, HfNO, and VNO. Furthermore, our calculations reveal a volcano-like relation between the limiting potential (U_L) and binding energy (BE) of ENRR intermediates identifying nitrogen binding energy (NBE) and N_2H binding energy (N_2HBE) as descriptors for ENRR activity on TMNO(100) surfaces.

1. INTRODUCTION

Ammonia (NH_3), currently being produced via the Haber-Bosch process,[1-6] is an essential chemical primarily used to manufacture fertilizers. The Haber-Bosch process takes place at high temperatures and pressures and consumes approximately 2% of the global energy, and contributes significantly to greenhouse gas emissions[7,8]. Because of the energy and carbon-intensive nature of this industrialized process, NH_3 and fertilizer production is typically carried out in a centralized plant, and the fertilizer is transported to agricultural farmlands where it will be used [9,10]. Thus, an alternative small-scale carbon and energy-efficient production of NH_3 would be highly beneficial to mitigate CO_2 emission and minimize the losses of reactive nitrogen in fertilizer due to transportation from the central plant to the agricultural fields[11].

Electrochemical nitrogen reduction reaction (ENRR) involves the reaction of nitrogen and hydrogen to produce ammonia and is beneficial compared to the Haber Bosch process because of the feasibility of this reaction under ambient conditions (i.e., room temperature and pressure)[12-18]. The ENRR process is anticipated to be carbon neutral when it is carried out using the electricity generated from renewable sources (e. g., electricity generated from solar and wind). Furthermore, a small-scale ENRR plant in local agricultural fields also eliminates the transportation problem associated with the centralized production of NH_3 and fertilizer. Thus, ENRR, which has recently gained significant research interest, represents a low-cost and carbon-efficient approach to producing an NH_3 alternative to the Haber Bosch process [19-21].

An active and selective catalyst that effectively converts N_2 to NH_3 at ambient conditions is required, besides many other components that need to be optimized for the development of ENRR technologies[22,23]. Particularly, the importance of an efficient catalyst is highlighted because of the need to break a strong triple bond of N_2 molecule (bond dissociation energy (945 KJ/mol)[24-

[27] to produce NH_3. Significant efforts, both experimental and theoretical, have been devoted to gaining a mechanistic understanding of ENRR and predicting and designing active and selective catalysts.[28-30] In recent years, noble metals[31-39] and non-noble metals,[40-44] including their oxides,[45-47] hydroxides,[48-50] nitrides,[51,52] carbides,[53-55] sulfides,[56,57] phosphides,[58,59] metal-organic frameworks (MOFs),[60,61] and single-atom catalysts[62,63] have been explored as catalysts for ENRR. Transition metal nitrides (TMNs), which represent an emerging class of materials currently being explored for application in energy storage and conversion, have gained significant attention as ENRR catalysts[55,64-67]. TMNs such as ZrN, NbN, CrN, and VN have been predicted to promote ENRR via the Mars-van Krevelen (MvK) mechanism at a low applied potential[68]. Along MvK mechanism, N atom on the surface is reduced to NH_3, creating a surface N-vacancy for the adsorption of N_2 and its reduction to NH_3.

Oxygen-modified TMNs i. e. transition metal oxynitrides (TMNOs) have been shown to selectively promote the ENRR via the MvK mechanism at low overpotential[69]. Our recent work on TMNO(111) surfaces has shown that surface N-vacancies, thermodynamically more favorable than the surface O-vacancies, are the active sites of ENRR. However, the structure sensitivity of TMNOs for ENRR remains unexplored. For example, how does the activity of nonpolar TMNO(100) compare to polar TMNO(111) surfaces? Can we tune the ENRR activity by surface engineering of TMNOs? What are the activity descriptors on TMNO(100)? In this study, we carry out extensive DFT calculations to study the ENRR activity on TMNO(100) surfaces for TM = Co, Cr, Cu, Fe, Hf, Mn, Nb, Ni, Sc, Ta, Ti, V, Y, Zn, Zr. In general, our DFT results show that the ENRR proceeds via the MvK mechanism on N-vacancy. Of all the TMNO(100) surfaces, our DFT calculations predict that MnNO, CrNO, FeNO, CuNO, HfNO and VNO are promising candidates for ENRR. Our results also indicate that nitrogen binding energy (NBE) and N_2H binding energy (N_2HBE) are descriptors for ENRR activity on TMNO(100) surfaces.

2. COMPUTATIONAL METHODS

All density functional theory (DFT)[70] calculations are performed using the Vienna Ab-Initio Simulation Package (VASP) code[71,72] at the GGA level within the PAW-PW91 formalism[73,74] and are spin-polarized.

The bulk structure of transition metal oxynitrides (TMNOs) in this study is modeled using the rocksalt structure with an oxygen (O) concentration of 25%. Nonpolar TMNO(100) surfaces are modeled using a 4 layer 2 × 2 surface slabs. Our modeled TMNO(100) surfaces contain TM, N and O atoms on the topmost surface layer, which allow us to investigate the ENRR on TM sites as well as surface N and O vacancies. We added a vacuum of approximately 15 Å to the surface in the z-direction to reduce the interactions between the surface and its periodic images.

During calculations, atoms in the bottom two layers are fixed while the atoms on the top two layers are allowed to relax until the Hellman-Feynman force on each ion is less than 0.02 eV/Å. A plane-wave basis set at cut-off energy of 400 eV is used to calculate the total energy, and a 3 × 3 × 1 Monkhrost-Pack grid is used to carry out the Brillion zone integration [75].

The binding energy (BE) of ENRR reaction intermediates is calculated as:

$$\mathrm{BE(intermediate)} = \mathrm{E(slab + intermediate)} - \mathrm{E(slab)} - \mathrm{E(intermediate)}$$

where E(slab + intermediate), E(slab), and E(intermediate) are the total energies of the slab with intermediate, clean slab, and reaction intermediates in the gas phase, respectively.

The computational hydrogen electrode (CHE) model[76] is used in computing the changes in free energy. Here, $\mu(H^+ + e^-)$, the chemical potential of a proton-electron pair equals ($1/2\mu(H_2)$), which is half of the chemical potential of H_2(g) at the applied potential (U) = 0 V.

Hence, we can calculate the sum of the chemical potential of the proton-electron pair as a function of U using the equation:

$\mu(H^+ + e^-) = 1/2\mu(H_2(g)) - eU$.

The CHE model is employed at U = 0 V to construct the free energy diagrams (ΔG vs. reaction coordinates) of the ENRR. The change in Gibbs free energy (ΔG) between the elementary steps is calculated as[76]

$\Delta G = \Delta E + \Delta ZPE - T\Delta S$

where ΔE is obtained from DFT calculations, ΔS and ZPE are the entropy and zero-point energy corrections (Table S1), respectively, and T = 298.15 K.

For kinetic modeling, we assume that the forward and backward steps are at equilibrium, and the rate of the forward reaction is written as[77]

$$r_1 = k_1(1 - \theta)C_{H+}$$

where k_1 is the rate constant, θ is the reaction intermediate coverage and C_{H+} is the proton concentration in the electrolyte.

The surface coverage (θ) of any of the reaction intermediates is defined as[77-79]

$$\theta = \frac{K}{1+K}$$

and,

$$K = \exp\left(-\Delta G/kT\right)$$

where K is the equilibrium constant for the reaction steps, k is the Boltzmann constant ($8.616 \times 10^{-5}\, eVK^{-1}$), and ΔG is the change in free energy of the rate-limiting step.

Since the rate of a chemical reaction is mainly dependent on the rate-limiting step, we build a simple model outlined by Norskov and his co-workers[77]. The rate constant is described as

$$k_1 = k_o \exp\left(-\frac{\Delta G}{kT}\right)$$

where k_1 is the rate constant when $\Delta G > 0$, $k_o$is the rate constant that represents the effect of solvent reorganization during the transfer of proton to the surface.

And the exchange current is $i_o = -er_1$. Therefore,

$$i_o = -ek_o \frac{1}{1 + \exp\left(-\Delta G/kT\right)} \exp\left(-\Delta G/kT\right)$$

where k_o is given by 1 $s^{-1}site^{-1}$ as used in previous studies.[78]

3. RESULTS AND DISCUSSION

Nonpolar TMNO(100) surfaces are the thermodynamically most stable surface termination for TMN in rocksalt crystal structures[80]. Thus, the experimentally synthesized TMN nanoparticles are expected to be composed of dominant (100) surface termination and most likely contribute to the overall catalytic activity of TMNs for reactions such as ENRR. Herein, we investigate the ENRR activity of TMNO(100) surfaces for TM = Co, Cr, Cu, Fe, Hf, Mn, Nb, Ni, Sc, Ta, Ti, V, Y, Zn, Zr). More specifically, we study the ENRR enabled by the perfect TM(100) surface as well as the surface N- and O-vacancies using the DFT calculations. Firstly, the possibility of the existence of surface vacancies (Figure S1) is examined. To this end, the vacancy formation energies of N- and O- vacancies are calculated using the reactions:

$$\mathrm{Surface} + 3/2\mathrm{H_2(g)} \rightarrow \mathrm{N-vaccancy} + \mathrm{NH_3(g)}$$

$$\mathrm{Surface} + \mathrm{H_2(g)} \rightarrow \mathrm{O-vacacancy} + \mathrm{H_2O(g)}$$

Our calculated vacancy formation energies in Figure 1 show that the energy required to form N-vac is smaller than that needed to form O-vac except on CrNO and NbNO. Thus, in general, N-vacancies are predicted to be thermodynamically more favorable to be formed compared to O-vacancies. Therefore, we limit our discussion of ENRR on perfect surfaces and N-vacancy sites as our calculations show that N-vacancies are energetically more favorable than O-vacancies. The results obtained on O-vacancy promoted ENRR are presented in the supporting information (SI).

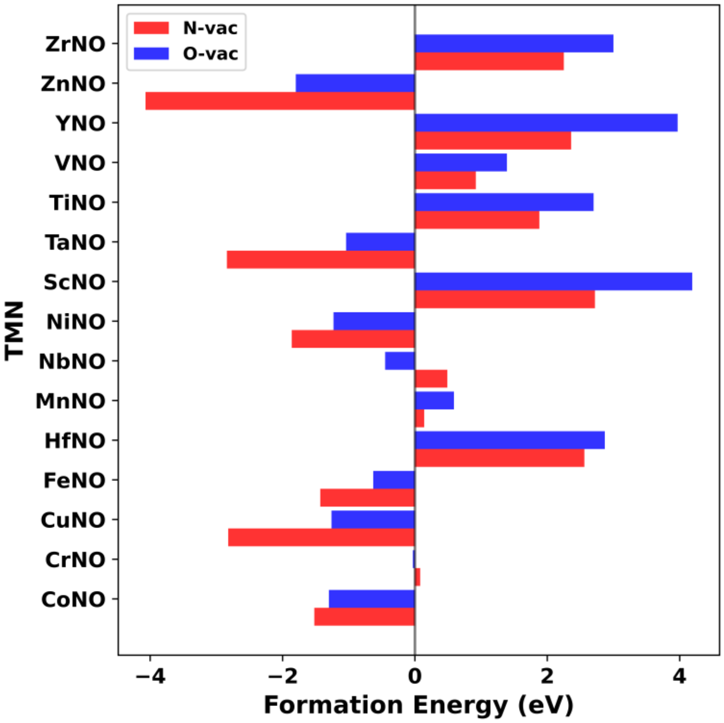

Figure 1. DFT calculated formation energies of N and O vacancies on TMNO(100) surfaces.

The ENRR has been shown to proceed along three pathways – distal, enzymatic, and alternating[81]. However, our recent study on TMNO(111) surfaces has shown that the ENRR mainly occurs along the distal channel via the dissociative pathway and or two associative pathways[69] as shown in Figure 2. The associative N_2H_2 pathway starts with the reduction of $*N_2$ to $*N_2H_2$, which dissociates upon (H^+ + e^-) transfer to produce *N + NH_3(g). Thus produced *N undergoes successive (H^+ + e^-) transfer to produce a second $*NH_3$. Finally, $*NH_3$ desorbs to form NH_3(g). Along the associative N_2H pathway, $*N_2H$ formed due to (H^+ + e^-) transfer undergoes N-N bond scission to produce *N + *NH. *N and *NH undergo (H^+ + e^-) transfer reactions to form $*NH_3$. The dissociative pathway is characterized by the dissociation of adsorbed N_2 molecule into 2 *N. *N then undergoes three reduction reactions to form $*NH_3$, which finally desorbs to form NH_3(g).

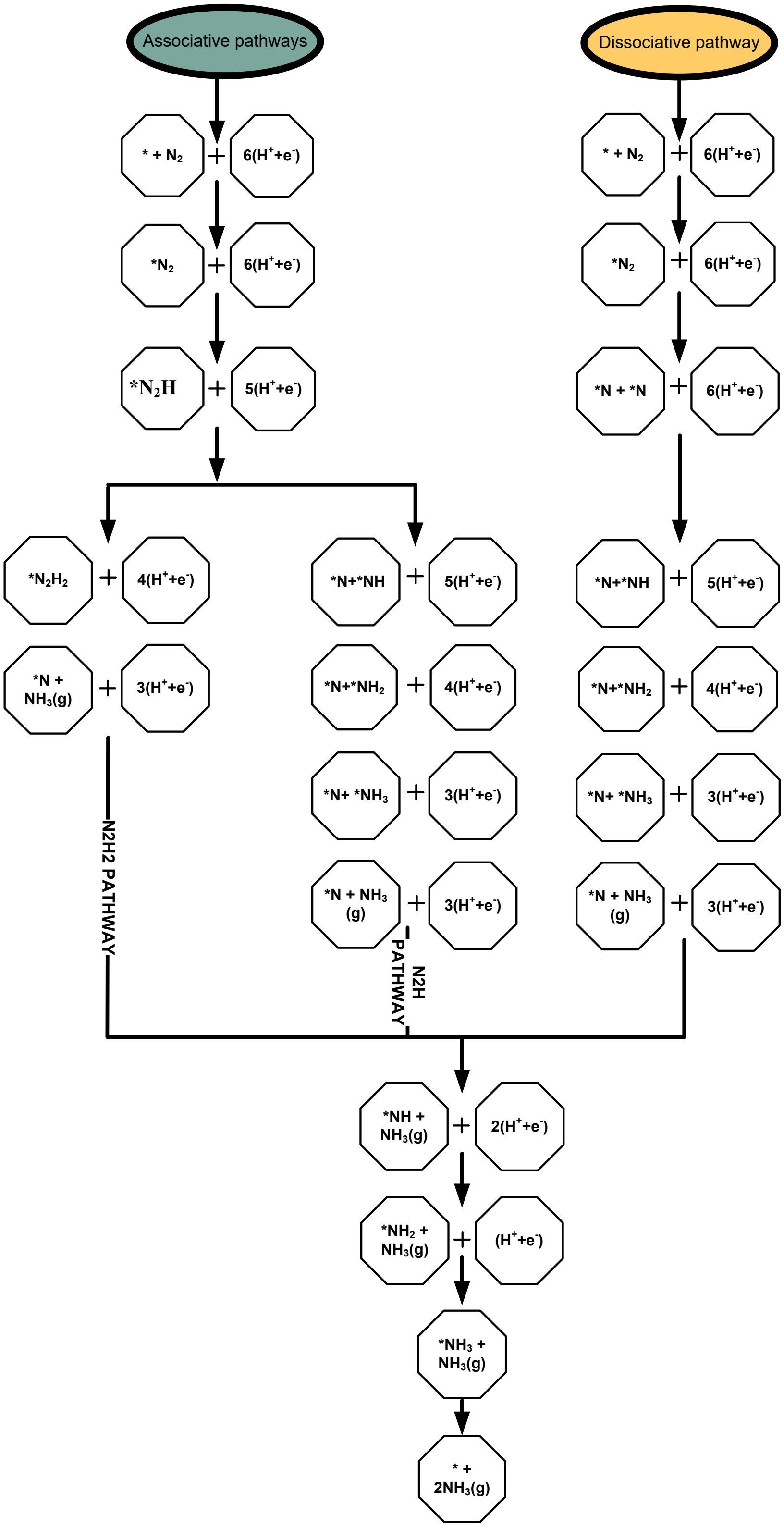

Figure 2. Three possible reaction pathways of ENRR. * =active site.

The binding energies of ENRR intermediates $^*N$, $^*N_2$, $^*N_2H$, $^*N_2H_2$, $^*NH$, $^*NH_2$, and $^*NH_3$ are calculated at their most favorable binding configurations on all possible sites of perfect TMNO(100) surfaces (TM = Co, Cr, Cu, Fe, Hf, Mn, Nb, Ni, Sc, Ta, Ti, V, Y, Zn, Zr) as well as on N-vacancy and O-vacancy sites. On perfect surfaces, reaction intermediates are bound at the metal sites (Figure S2), while the reaction intermediates are bound at the vacancy sites on the surfaces with N and O vacancies. In general, as expected, we find that the surface vacancies stabilize the reaction intermediates (Figure S3) compared to the perfect TMNO(100) surfaces where the ENRR intermediates are bound at metal sites. Additionally, the DFT calculated binding energies in Figure S4 demonstrate that most of the reaction intermediates bind more strongly to O-vac compared to the N-vac and perfect surfaces.

3.1 ENRR on perfect TMNO(100) surfaces

The DFT computed binding energies are used to calculate the change in free energies (ΔG) at an applied U = 0 V using the CHE model along the three different reaction pathways shown in Figure 2. Figures 3, 4, and 5 (made using Origin pro) show the ΔG along N_2H_2 associative pathway, N_2H associative pathway, and the dissociative pathway on the perfect TMNO(100) surfaces (Tables S2-S7).

Along the associative N_2H_2 pathway, we observed from Figure 3 that the overall ENRR activity of CuNO and NiNO is limited by the formation of $^*N_2H$ from the elementary step: $^*N_2 + (H^+ + e^-) \rightarrow {}^*N_2H$. On CuNO and NiNO, the ΔG values of this step are calculated to be 1.88 eV and 1.67 eV, respectively. The rate-limiting steps (most difficult steps) on CrNO and NbNO along the associative N_2H_2 pathway are predicted to be $^*N_2H + (H^+ + e^-) \rightarrow {}^*N_2H_2$ and $^*NH_3 \rightarrow {}^* + NH_3(g)$ with ΔG values of 1.38 eV and 1.98 eV, respectively. In contrast, on FeNO, HfNO, MnNO, ScNO, TiNO, VNO, YNO, and ZrNO the rate-limiting step is predicted to be $^*N_2 + (H^+$

+ e^-) → *N_2H, and has ΔG values of 1.38 eV, 1.17 eV, 1.43 eV, 1.61 eV, 1.52 eV, 0.95 eV, 1.45 eV, and 1.37 eV respectively. The results show that ENRR on most of the perfect TMNO(100) surfaces via the associative N_2H_2 pathway is sluggish due to the high ΔG values of the rate-limiting steps. Comparing all the TMNOs in the present study, VNO has the lowest ΔG (0.95 eV) for the rate-limiting step.

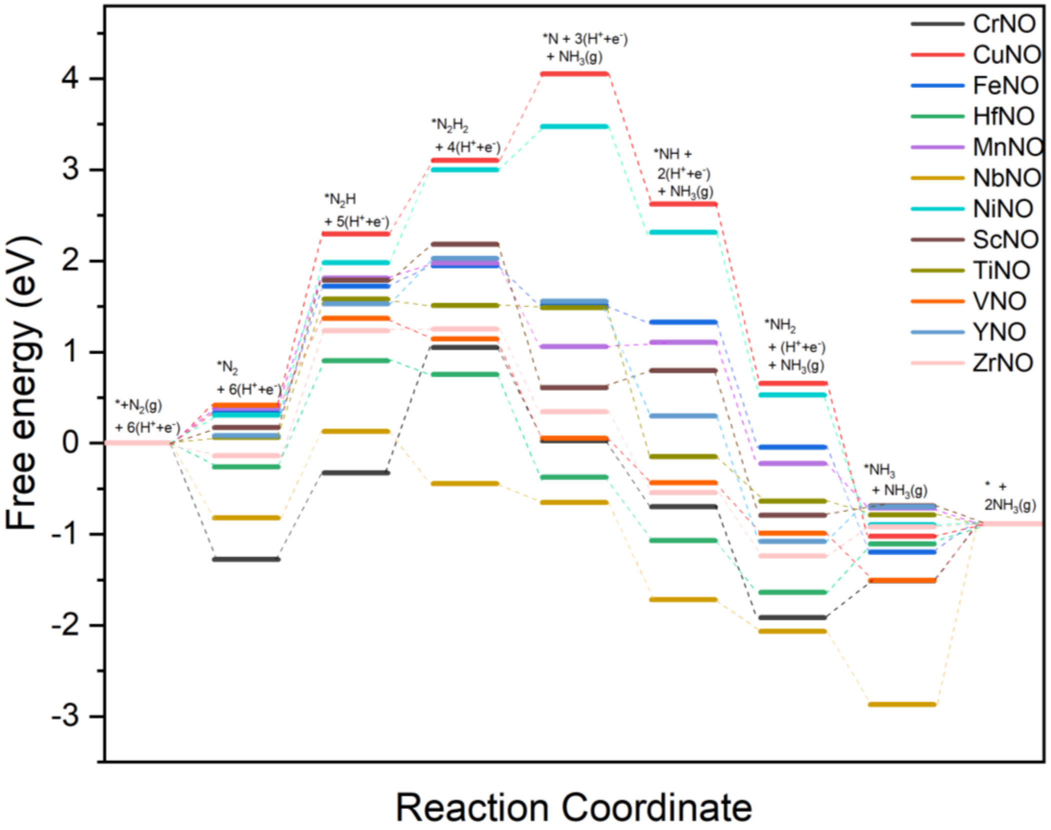

Figure 3. DFT calculated free energy diagrams of ENRR at U = 0 V along the associative N_2H_2 pathway on perfect TMNO(100) surfaces.

Figure 4 shows the ΔG of ENRR calculated along the associative N_2H pathway. It can be seen in Figure 4 that along the associative N_2H pathway, the formation of *N from the step: *N_2H + * → *N + *NH is predicted to be rate-limiting on CuNO, NiNO, and FeNO with ΔG of 5.27 eV, 4.69 eV, and 2.00 eV, respectively. In contrast, the rate-limiting step along the associative N_2H

pathway on NbNO is $^*NH_3 \rightarrow\ ^* + NH_3(g)$ with a ΔG value of 1.98 eV. On the other hand, the rate-limiting step on CrNO, HfNO, MnNO, ScNO, TiNO, VNO, YNO, and ZrNO is found to be $^*N_2 + (H^+ + e^-) \rightarrow {}^*N_2H$, and has ΔG values of 0.95 eV, 1.17 eV, 1.43 eV, 1.61 eV, 1.52 eV, 0.95 eV, 1.45 eV, and 1.37 eV respectively. The relatively high ΔG indicates that the ENRR most likely does not proceed via the associative N_2H pathway on TMNO(100) surfaces.

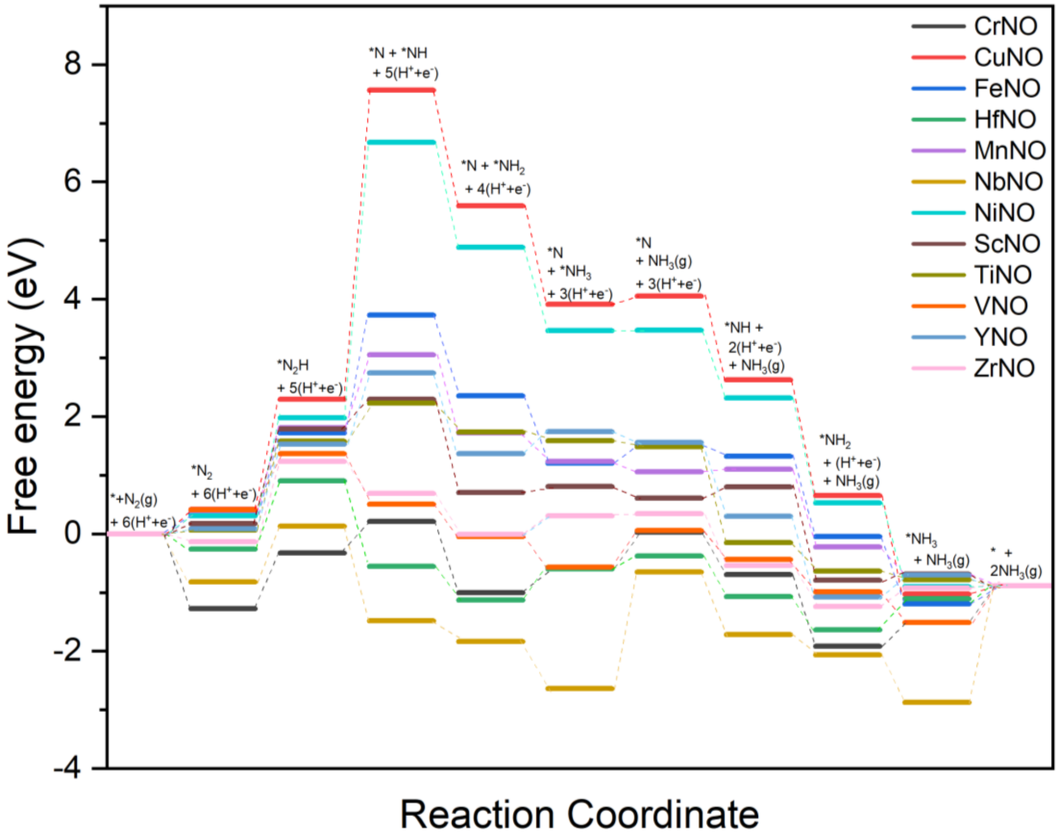

Figure 4. DFT calculated free energy diagrams of ENRR at U = 0 V along the associative N_2H pathway on perfect TMNO(100) surfaces.

Figure 5 shows the DFT calculated ΔG along the dissociative pathway on perfect TMNO(100) surfaces. Dissociation of N_2 to 2*N, a non-electrochemical step, is determined to be the rate-limiting step on CrNO, CuNO, FeNO, MnNO, NiNO, ScNO, TiNO, YNO, and ZrNO with an uphill energy barrier of 2.22 eV, 8.57 eV, 3.58 eV, 2.62 eV, 7.52 eV, 1.93 eV, 3.80 eV, 3.92

eV, and 1.71 eV respectively. Our DFT calculations predict that the rate limiting steps on HfNO, NbNO, and VNO are $*NH_2 + (H^+ + e^-) \rightarrow *NH_3$, $*NH_3 \rightarrow * + NH_3(g)$, and $*NH_3 \rightarrow * + NH_3(g)$ with ΔG values of 0.53 eV, 1.98 eV, and 0.62 eV respectively.

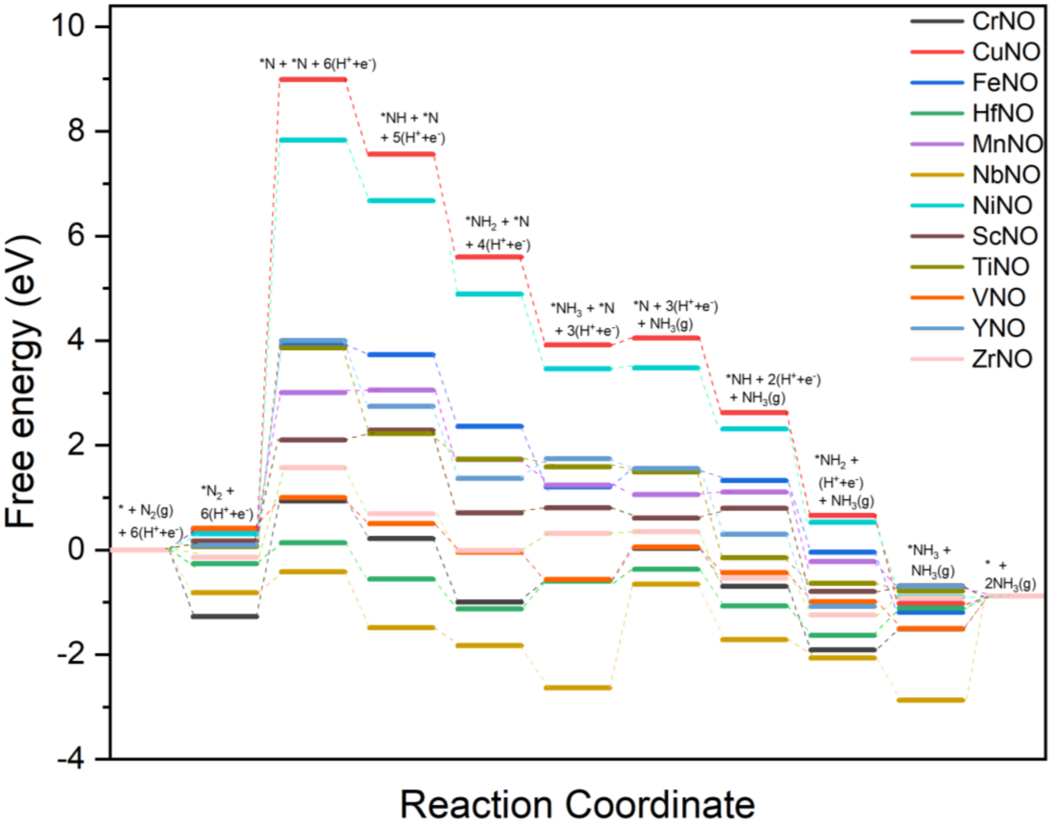

Figure 5. DFT calculated free energy diagrams of ENRR at U = 0 V along the Dissociative pathway on perfect

Comparing Figures 3, 4 and 5, it is seen that ENRR proceeds more favorably via the associative N_2H_2 pathway on CuNO, FeNO, MnNO, NiNO, ScNO, TiNO, YNO. The ΔG values of the rate-limiting steps on CuNO, FeNO, MnNO, NiNO, ScNO, TiNO, and YNO are predicted to be 1.88 eV, 1.38eV, 1.42eV, 1.67 eV, 1.61 eV, and 1.44 eV, respectively. On the other hand, the ENRR proceeds along the N_2H associative pathway on CrNO and ZrNO and the ΔG values of the rate-limiting steps are calculated to be 0.95 eV and 1.37 eV, respectively. The dissociative pathway is found to be the most favorable pathway on NbNO, HfNO, and VNO, with ΔG of 1.98 eV, 0.53 eV, and 0.62 eV for the rate-limiting step. Our DFT calculations predict the smallest ΔG values of the rate-limiting step on HfNO and VNO. Therefore, the metal sites on perfect HfNO(100) and VNO(100) are predicted to promote the ENRR at low applied U. Interestingly, the result obtained on VNO(100) from this study is similar to our previous DFT results on VNO(111) and experimental results on VNO catalysts[82].

Limiting potential (U_L), an applied U at which all the electrochemical steps are downhill in ΔG, is calculated using the free energy diagrams in Figures 3, 4 and 5 along the DFT predicted most favorable pathways on TMNO(100) surfaces. Our calculated U_L values are -0.95 V, -1.88 V, -1.38 V, -0.53 V, -1.43 V, 0 V, -1.67 V, -1.61 V, -1.52 V, 0 V, -1.45 V, and -1.37 V on CrNO, CuNO, FeNO, HfNO, MnNO, NbNO, NiNO, ScNO, TiNO, VNO, YNO, and ZrNO, respectively. The computed U_L values along the most favorable reaction pathways are plotted against the N_2H binding energies (BEs). The results reveal a volcano-like relationship with N_2HBE as shown in Figure 6. The U_L computed on NbNO, VNO, and HfNO are the smallest and lie close to the top of the volcano. This implies that NbNO, VNO, and HfNO are promising candidates for N_2 reduction to NH_3. The volcano-like plot in Figure 4 also shows that CuNO, NiNO, MnNO, FeNO, VNO, ScNO, TiNO, YNO, ZrNO, and HfNO bind N_2H weakly, and their U_L values lie to the right of the volcano while N_2H binds too strongly on CrNO. Importantly, our DFT calculations suggest that N_2HBE can be used as a descriptor of the ENRR activity on TMNO(100) surfaces.

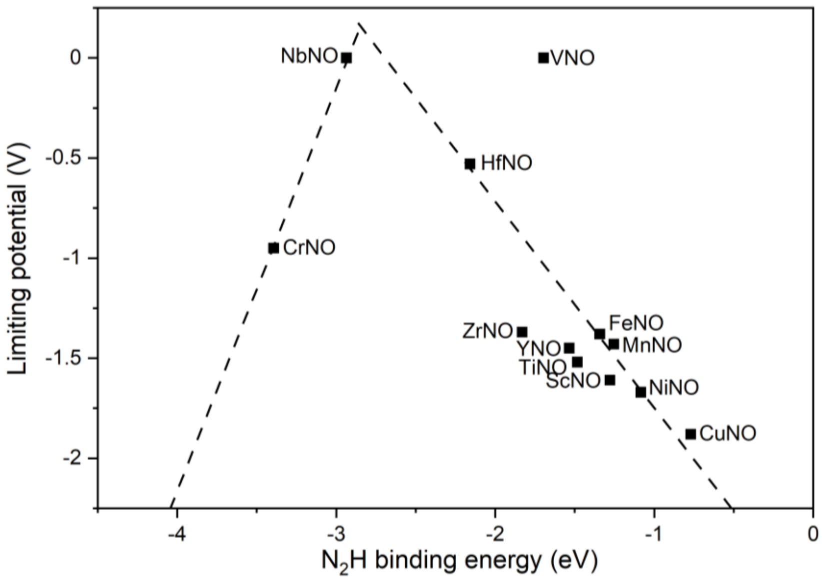

Figure 6. A plot between N_2H binding energy (N_2HBE) and U_L along the most favorable ENRR pathways on perfect TMNO(100) surfaces.

3.2 ENRR on N-vacancies of TMNO(100) surfaces

Previous DFT and experimental studies have indicated that the adsorption of N_2 and its conversion to NH_3 on TMN-based catalysts is promoted by the presence of N-vacancies [69,83-86]. The presence of N- vacancies on TMN surfaces enhances the binding affinity of reaction intermediates and lowers the energy barrier for the breaking of the N-N bond, an essential step for the conversion of N_2 to NH_3[10,23]. However, studies aiming to unravel the vacancy-mediated ENRR on TMNO(100) are currently lacking. In an attempt to fulfill this knowledge gap, herein, we perform DFT calculations to study vacancy-mediated ENRR on TMNO(100) surface. The DFT calculated binding energies (Figure S4) are used to construct the free energy diagrams along the three ENRR pathways shown in Figure 2.

Along the associative N_2H_2 pathway, the DFT computed free energy diagrams in Figure 7 show that the step: $*N_2H + (H^+ + e^-) \rightarrow *N_2H_2$ is predicted to be rate-limiting on CrNO, CuNO, NiNO, TiNO, VNO, and ZrNO with ΔG values of 1.05 eV, 0.61 eV, 1.36 eV, 1.04 eV, 0.92 eV, and 1.35 eV, respectively. In contrast, the rate-limiting step is predicted to be the step $*NH + (H^+ + e^-) \rightarrow *NH_2$ on HfNO, ScNO, and YNO with ΔG values of 1.13 eV, 1.99 eV and 1.86 eV, respectively. Different from the N_2H_2 and NH_2 formation steps as the rate-limiting, our calculations predict that the rate-limiting step on FeNO is the step: $N_2 + (H^+ + e^-) \rightarrow * N_2H$ having ΔG value of 0.52 eV. Finally, on MnNO, the adsorption of $*N_2$ is predicted to be the rate-limiting step with a ΔG value of 1.0 eV.

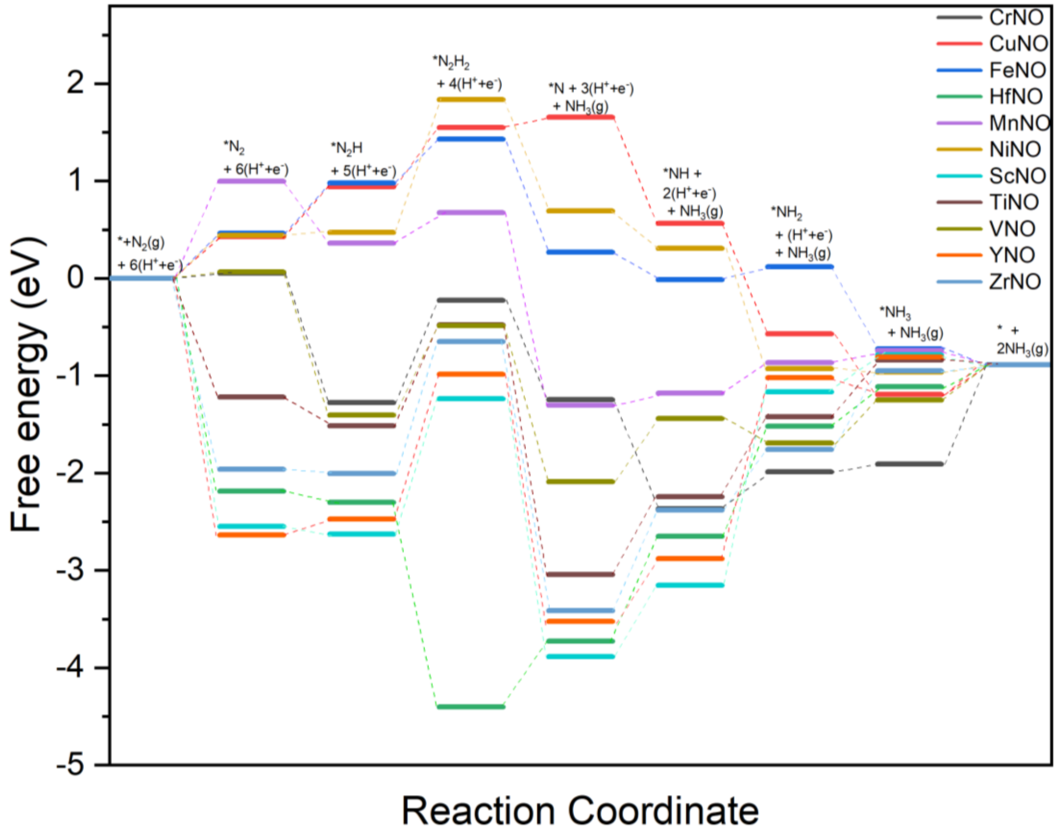

Figure 7. DFT calculated free energy diagrams of ENRR at U = 0 V along the associative N_2H_2 pathway on N-vacancies present on TMNO(100) surfaces.

Figure 8 displays the ΔG values of reaction steps along the associative N_2H pathway. The dissociation of N_2H to form *NH in the step: $*N_2H \rightarrow *N + *NH$ is predicted to be the rate-limiting step on CuNO and NiNO, with ΔG values of 2.17 eV and 1.42 eV, respectively. However, on HfNO, ScNO, TiNO, and YNO, the rate-limiting step is predicted to be the formation of $*NH_2$ i. e. $*NH + (H^+ + e^-) \rightarrow *NH_2$ with ΔG values of 1.13 eV, 1.99 eV, 0.82 eV, and 1.86 eV, respectively. Similarly, the rate-limiting step on VNO and ZrNO is found to be the formation of *NH from the step: $N + (H^+ + e^-) \rightarrow *\ NH$ with ΔG values of 0.65 eV and 1.04 eV, respectively. On MnNO, the adsorption of $*N_2$ is predicted to be the rate-limiting step with a ΔG value of 1.0 eV, whereas the desorption of $*NH_3$ is the rate-limiting step on CrNO with a ΔG value of 1.02 eV.

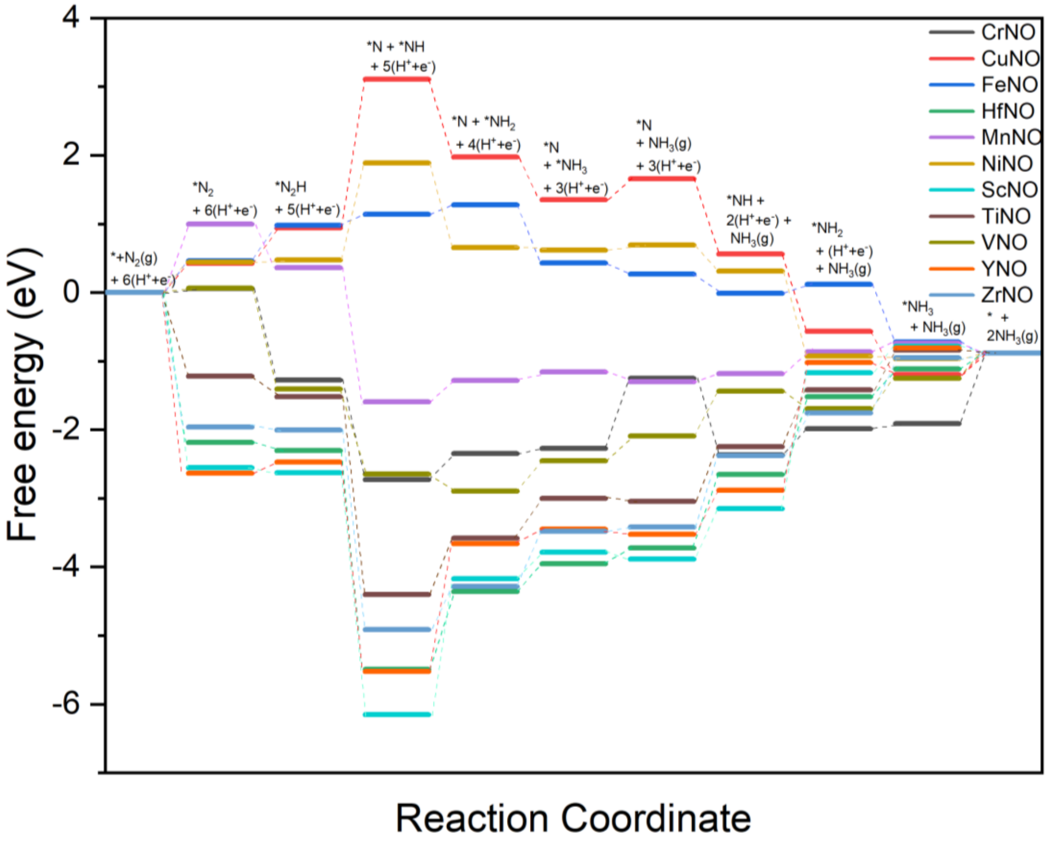

Figure 8. DFT calculated free energy diagrams of ENRR at U = 0 V along the associative N_2H pathway on N-vacancies present on TMNO(100) surfaces.

The DFT calculated ΔG along the dissociative pathway is presented in Figure 9. It can be seen in Figure 9 that along the dissociative pathway, the dissociation of $*N_2$ to form *N and *N i.

e. the step $*N_2 \rightarrow *N + *N$ is predicted to be the rate-limiting step on CuNO, FeNO, NiNO, with ΔG values of 3.77 eV, 0.96 eV, and 1.83 eV, respectively. On HfNO, ScNO, TiNO, and YNO, the rate-limiting step is the formation of $*NH_2$ i. e. the step: $*NH + (H^+ + e^-) \rightarrow *NH_2$ with ΔG values of 1.13 eV, 1.99 eV, 0.82 eV, and 1.86 eV, respectively. The rate-limiting step on VNO and ZrNO is the formation of *NH i. e. the step: $N + (H^+ + e^-) \rightarrow *NH$ with ΔG values of 0.65 eV and 1.04 eV, respectively. On MnNO, the adsorption of $*N_2$ i. e., the step: $N_2 + * \rightarrow * N_2$ is predicted to be the rate-limiting step with a ΔG value of 1.0 eV. Finally, the desorption of $*NH_3$ is the rate-limiting step on CrNO with a ΔG value of 1.02 eV.

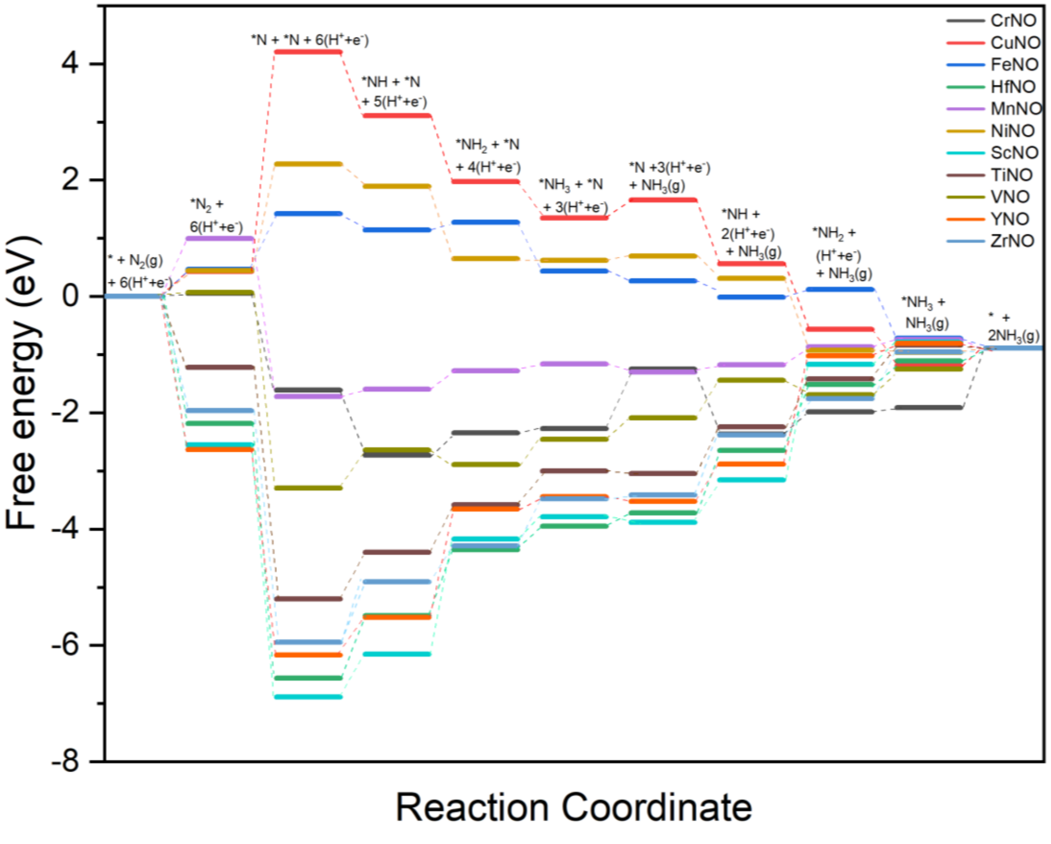

Figure 9. DFT calculated free energy diagrams of ENRR at U = 0 V along the dissociative pathway on N-vacancies present on TMNO(100) surfaces.

Comparing the free energy diagrams in Figures 7, 8, and 9, it is found that the N-vacancy promoted ENRR proceeds along the associative N_2H pathway on FeNO, HfNO, MnNO, ScNO, TiNO, VNO, and ZrNO with ΔG values for the rate-limiting steps of 0.52 eV, 1.13 eV, 1.00 eV, 1.99 eV, 0.82 eV, 0.65 eV, and 1.04 eV, respectively. The rate-limiting steps along the associative N_2H pathway are predicted to be $*N_2 + (H^+ + e^-) \rightarrow *N_2H$, $*NH + (H^+ + e^-) \rightarrow *NH_2$, $* + N_2 \rightarrow *N_2$, $*NH + (H^+ + e^-) \rightarrow *NH_2$, $*NH + (H^+ + e^-) \rightarrow *NH_2$, $*N + *NH_3 \rightarrow *NH$, and $*N + (H^+ + e^-) \rightarrow *NH$ on FeNO, HfNO, MnNO, ScNO, TiNO, VNO, and ZrNO, respectively. In contrast, CuNO and NiNO the ENRR most likely proceeds along the associative N_2H_2 pathway with ΔG values of the rate-limiting step ($*N_2H + (H^+ + e^-) \rightarrow *N_2H_2$) of 0.61 eV and 1.36 eV, respectively. YNO is predicted to promote the ENRR along the dissociative pathway with a ΔG value of the rate-limiting step ($*NH + (H^+ + e^-) \rightarrow *NH_2$) of 1.86 eV.

The DFT predicted U_L values via the most favorable pathways on CrNO, CuNO, FeNO, HfNO, MnNO, NiNO, ScNO, TiNO, VNO, YNO, and ZrNO are -0.38V, -0.61 V, -0.52 V, -1.13 V, -0.31 V, -1.36 V, -1.99 V, -0.82 V, -0.65 V, -1.86 V, and -1.04 V, respectively. Here, our calculations predict that the electrochemical steps on CuNO, FeNO, HfNO, NiNO, ScNO, TiNO, YNO, and ZrNO have larger ΔG values than the most difficult non-electrochemical steps except for MnNO where the non-electrochemical step is predicted to be the rate-limiting of the ENRR. The computed U_L values along the most favorable reaction pathways were plotted against the N binding energies (NBE). A volcano-like relationship is also observed between the computed U_L values and the NBE (Figure 10). The U_L computed on MnNO, CrNO, FeNO, CuNO, TiNO, and VNO are the lowest (below 1 V) and lie close to the top of the volcano. This implies that MnNO, CrNO, FeNO, CuNO, and VNO are promising candidates for N_2 reduction to NH_3. The volcano-like plot in Figure 10 also shows that YNO, ScNO, HfNO, ZrNO, and TiNO lie to the left of the volcano plot and bind N stronger compared to MnNO, CrNO, FeNO, CuNO, and VNO. Thus, our DFT calculations suggest that NBE is a descriptor of the N-vacancy mediated ENRR activity on TMNO (100) based catalysts.

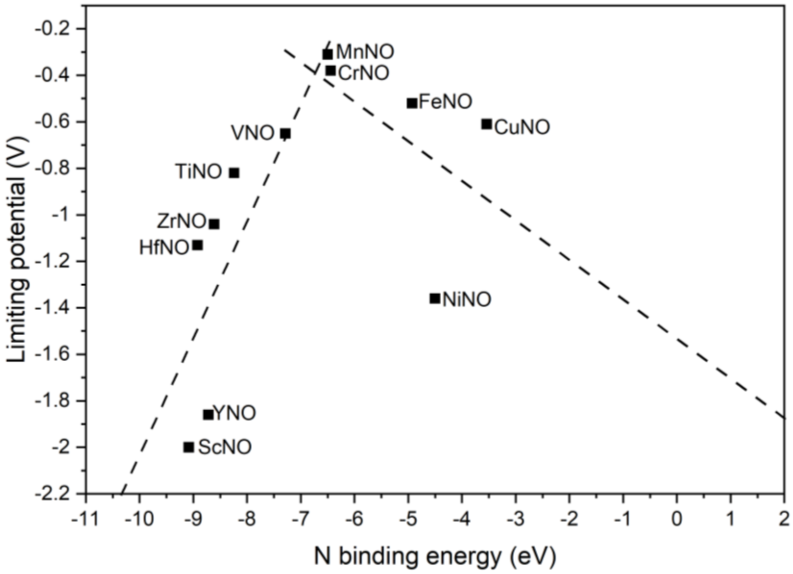

Figure 10. A plot between N binding energy (NBE) and U_L along the most favorable ENRR on N-vacancies present on TMNO(100) surfaces.

The smaller U_L values of ENRR on perfect and N-vacancies present TMNO(100) for TM = V, Nb and Hf show that the metal sites as well as N-vacancies on (100) surfaces of VNO, NbNO, and HfNO are capable of promoting the ENRR at low U. Thus, the ENRR activity of these candidates may be arising from the meal sites as well as any surface N-vacancies. Interestingly, the DFT calculated U_L values on the (100) surfaces of MnNO, CrNO, FeNO, CuNO, and VNO (-0.31 V, -0.38 V, -0.52 V, -0.61 V, and -0.65 V) are comparable to the U_L values calculated on (111) surfaces of MnNO, TiNO, and VNO (-0.28 V, -0.42 V, and -0.18 V)[69]. This suggests that N-vacancies on (111) and (100) surfaces offer similar ENRR activity for MnNO and VNO. As a result, experimental synthesis of TMNO nanoparticles predominantly containing (111) and (100) facets could be a helpful strategy to optimize the ENRR activity of our DFT predicted promising candidates: MnNO, TiNO, and VNO. The additional density of states (DOS) calculations performed on select TMNOs (Figure S8) pinpoint that the TMNOs that have more states near the fermi level (e.g., CuNO and VNO) show enhanced ENRR performance compared to the candidates that have lower states available at the Fermi level (e. g., (ScNO and YNO).

3.3 ENRR on O-vacancies of TMNO(100) surfaces

The DFT calculated ΔGs along various ENRR pathways on O-vac are shown in Figures S5-S7. It is found the rate-limiting steps on CuNO, HfNO, MnNO, NiNO, ScNO, TiNO, VNO, YNO, and ZrNO on the most favorable pathways are $*N_2 + (H^+ + e^-) \rightarrow *N_2H$, $*N + (H^+ + e^-) \rightarrow *NH$, $*NH + (H^+ + e^-) \rightarrow *NH_2$, $*N_2 + (H^+ + e^-) \rightarrow *N_2H$, $*NH + (H^+ + e^-) \rightarrow *NH_2$, $*N + (H^+ + e^-) \rightarrow *NH$, $*NH + (H^+ + e^-) \rightarrow *NH_2$, $*NH + (H^+ + e^-) \rightarrow *NH_2$, and $*N + (H^+ + e^-) \rightarrow *NH$ respectively. The corresponding ΔG values for the rate-limiting steps on the most favorable pathways are 1.44 eV, 1.03 eV, 1.71 eV, 0.50 eV, 2.03 eV, 1.31 eV, 0.87 eV, 2.10 eV, and 1.34 eV on CuNO, HfNO, MnNO, NiNO, ScNO, TiNO, VNO, YNO, and ZrNO, respectively. The relatively low value of ΔG associated with the rate-limiting step results suggests that O-vacancies on NiNO and VNO promotes the ENRR at low applied U.

3.4 Microkinetic modeling

Microkinetic modeling of ENRR is performed along the DFT predicted most favorable ENRR pathways on TMNO(100) with and without N-vacancy using the methods described in the computational methods section and elsewhere.[79,87,88] On perfect TMNO(100), CrNO, HfNO, and VNO lie close to the regions where $\log(i_0)$ is maximum. Figure 11(a) shows that a catalyst that has N_2HBE of ~-2 eV and N_2BE of ~-1.6 would be ideal for optimum ENRR. However, Figure 11(a) also shows that N_2 and N_2H BE are linearly scaled. Thus, the breaking of the binding energy linear scaling is necessary to achieve the optimized ENRR on TMNO-based catalysts. The results in Figure 11(b) show that MnNO, CrNO, FeNO, CuNO, and VNO are close to the region with the highest ENRR current density. For N-vacancy mediated ENRR, the results obtained from microkinetic modeling in Figure 11(b) shows that the ENRR activity maximum occurs when a catalyst has N and N_2H BEs of ~-9 eV and -4.5 eV, respectively, on surface N-vacancies. Since NBE and N_2HBE are dependent on each other due to the linear scaling relation between them, independent tuning of NBE and N_2HBE is necessary to achieve maximum ENRR current density on TMNOs. Overall, the results from this study show that the ENRR efficiently occurs on (100) surfaces of MnNO, CrNO, FeNO, CuNO, and VNO at relatively low U. Thus, our DFT calculations predict that MnNO, CrNO, FeNO, CuNO, and VNO are promising candidates for enhanced ENRR among all the TMNOs included in the present study.

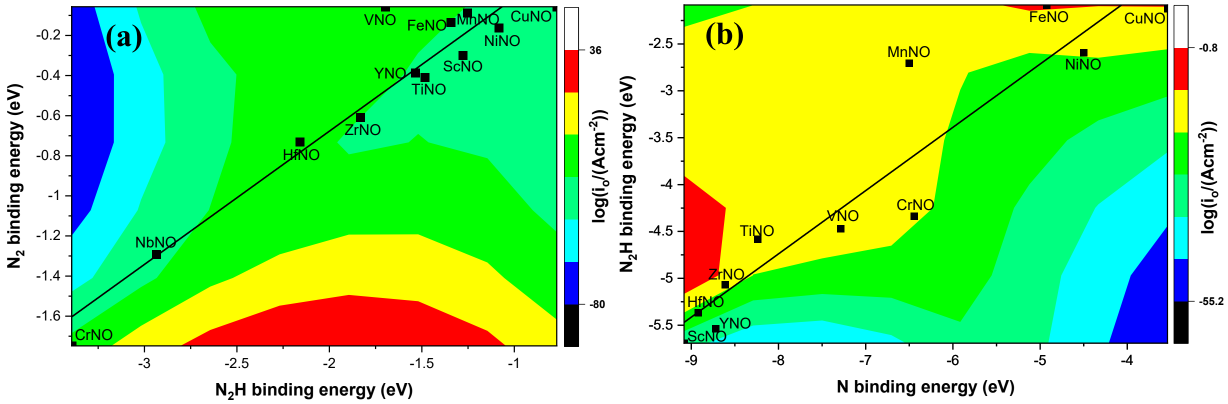

Figure 11. (a) Kinetic volcano of ENRR at U= 0 V on: (a) perfect TMNO (100) surfaces and (b) TMNO (100) surfaces with N-vacancies.

Hydrogen evolution reaction (HER) is a competing reaction with ENRR. The DFT calculated hydrogen binding energies (HBEs) are used to calculate the ΔG and UL values (Figures S9 and S10) to study the HER trends. The results show that HfNO, ZrNO, and MnNO lie close to the top of the volcano and are predicted to be the best candidates for HER. A comparison between the UL values of ENRR and HER in Figure 12 shows that of all perfect TMNOs included in the present study, VNO, HfNO, NbNO, and CrNO are the best candidates for ENRR. Similarly, MnNO, FeNO, and CuNO are predicted to be selective to ENRR for N-vac mediated ammonia production.

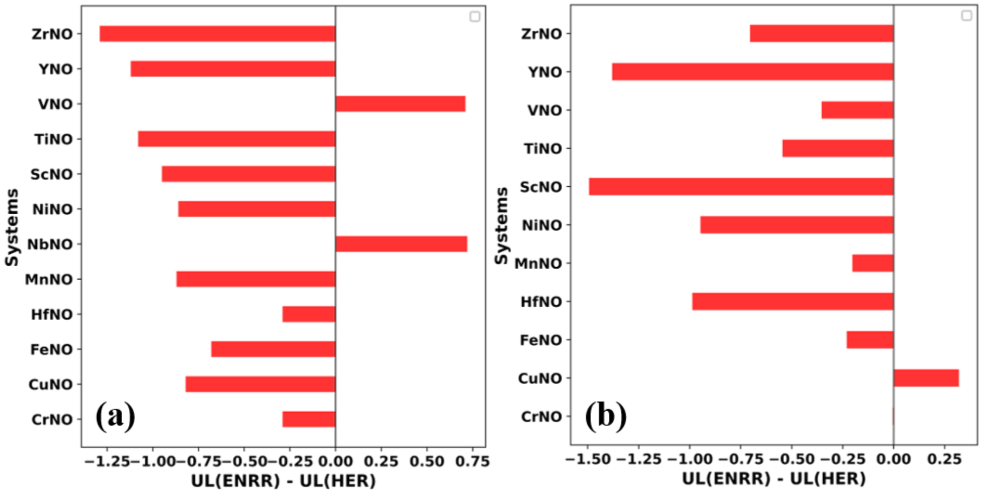

Figure 12. U_L(ENRR) - U_L(HER) on (a) perfect TMNOs(100) and (b) TMNOs(100) with N-vac.

4. CONCLUSIONS

DFT calculations are performed to study the ENRR on (100) surfaces of TMNOs for TM = Co, Cr, Cu, Fe, Hf, Mn, Nb, Ni, Sc, Ta, Ti, V, Y, Zn, Zr. In general, our calculated vacancy formation energies indicate that N-vacancies are thermodynamically more favorable compared to O-vacancies suggesting the existence of N-vacancies on TMNO(100) surfaces under experimental reaction conditions. The mechanistic investigation of ENRR along various pathways using the DFT calculated free energy change shows that metal sites as well as N-vacancies on (100) surface of VNO, NbNO, and HfNO are capable of promoting the ENRR at low U. However, the DFT calculations predict that N-vacancies are the preferred sites for enhanced ENRR (via MvK mechanism) on MnNO, CrNO, FeNO, CuNO, and TiNO. In addition, microkinetic modeling performed using the DFT energetics demonstrates that a perfect TMNO(100) surface that has

N_2HBE of ~-2 eV and N_2BE of ~-1.6 would be an ideal surface for maximized ENRR. Microkinetic modeling on TMNO(100) surfaces with N-vacancies reveals that an ideal catalyst for ENRR will have N and N_2H BEs of ~-9 eV and -4.5 eV, respectively. Our computed U_L values reveal a volcano-like relationship with NBE on perfect TMNO and N_2HBE on N-vac TMNO, which indicates that NBE and N_2HBE are potential descriptors of ENRR on TMNO (100) surfaces. Interestingly, the DFT calculated U_L values on the (100) surfaces of MnNO, CrNO, FeNO, CuNO, and VNO are comparable to the U_L values calculated on (111) surfaces of MnNO, TiNO, and VNO, illustrating that (111) and (100) surfaces offer similar ENRR activity for MnNO and VNO.

ASSOCIATED CONTENT

Supporting Information

The Supporting Information is available free of charge at ……..

Geometries of slab models and reaction intermediates adsorbed on models, Binding energies figures, ENRR free energy diagrams calculated on O-vacancies, DOS plots, HER free energy diagrams, Tables containing ZPE and TΔS values and ΔG values.

ACKNOWLEDGEMENTS

This work was partially supported by National Science Foundation Research Initiation Award (HRD 2055012) grant. The DFT calculations were performed using computational resources at the Extreme Science and Engineering Discovery Environment, which is supported by the National Science Foundation Grant number ACI-1548562.

REFERENCES

1. Ma, B.; Zhao, H.; Li, T.; Liu, Q.; Luo, Y.; Li, C.; Lu, S.; Asiri, A. M.; Ma, D.; Sun, X. Iron-group electrocatalysts for ambient nitrogen reduction reaction in aqueous media. *Nano Res.*, **2021**, 14, 555–569.

2. Schlögl, R. Catalytic Synthesis of Ammonia—A "Never-Ending Story"? *Angew. Chem. Int. Ed.*, **2003**, 42, 2004-2008.
3. Zhang, R.; Ren, X.; Shi, X.; Xie, F.; Zheng, B.; Guo, X.; Sun, X. Enabling Effective Electrocatalytic N_2 Conversion to NH_3 by the TiO_2 Nanosheets Array under Ambient Conditions. *ACS Appl. Mater. Interfaces*, **2018**, 10, 28251–28255.
4. Ding, Y.; Zhang, J.; Guan, A.; Wang, Q.; Li, S.; Al-Enizi, A. M.; Qian, L.; Zhang, L.; Promoting N_2 electroreduction to ammonia by fluorine-terminating $Ti_3C_2T_x$ MXene. *Nano Converg.*, **2021**, 8, 14.
5. Wang, L. Xia, M.; Wang, H.; Huang, K.; Qian, C.; Maravelias, C.T.; Ozin, G.A.; Greening Ammonia toward the Solar Ammonia Refinery. *Joule*, **2018**, 2, 1055–1074.
6. Garagounis, I.; Kyriakou, V.; Skodra, A.; Vasileiou, E.; Stoukides, M.; Electrochemical synthesis of ammonia in solid electrolyte cells. *Front. Energy Res.*, **2014**, 2, 1.
7. Yao, Y.; Wang, H.; Yuan, X.; Li, H.; Shao, M.; Electrochemical Nitrogen Reduction Reaction on Ruthenium. *ACS Energy Lett.*, **2019**, 4, 1336-1341.
8. Schiffer, Z.J.; Manthiram, K.; Electrification and decarbonization of the chemical industry *Joule*, **2017**, 1, 10-14.
9. McEnaney, J.M.; Singh, A. R.; Schwalbe, J.A.; Kibsgaard, J.; Lin, J.C.; Cargnello, M.; Jaramillo, T. F.; Norskov, J. K.; Ammonia synthesis from N2 and H2O using a lithium cycling electrification strategy at atmospheric pressure. *Energy Environ. Sci.,* **2017**, 10, 1621-1630.
10. Yang, X.; Nash, J.; Anibal, J.; Dunwell, M.; Kattel, S.; Stavitski, E.; Attenkofer, K.; Chen, J. G.; Yan, Y.; Xu, B. Mechanistic Insights into Electrochemical Nitrogen Reduction Reaction on Vanadium Nitride Nanoparticles. *J. Am. Chem. Soc.*, **2018**, 140, 13387-13391.
11. Montoya, J. H.; Tsai, C.; Vojvodic, A.; Norskov, J. K.; The Challenge of Electrochemical Ammonia Synthesis: A New Perspective on the Role of Nitrogen Scaling Relations. *ChemSusChem*, **2015**, 8, 2180-2186.
12. Ge, L.; Xu, W.; Chen, C.; Tang, C.; Xu, L.; Chen, Z.; Rational Prediction of Single Metal Atom Supported on Two-Dimensional Metal Diborides for Electrocatalytic N_2 Reduction Reaction with Integrated Descriptor. *J. Phys. Chem., Lett.,* **2020**, 11, 5241-5247.

13. Qing, G.; Ghazfar, R.; Jackowski, S. T.; Habibzadeh, F.; Ashtiani, M. M.; Chen, C.; Smith III, M. R.; Hamann, T. W.; Recent Advances and Challenges of Electrocatalytic N_2 Reduction to Ammonia. *Chem. Rev.*, **2020**, 120, 5437-5516.
14. Li, M.; Cui, Y.; Sun, L.; Zhang, X.; Peng, L.; Huang, Y.; Boosting Electrocatalytic N_2 Reduction to NH_3 over Two-Dimensional Gallium Selenide by Defect-Size Engineering. *Inorg. Chem.*, **2020**, 59, 4858-4867.
15. Peng, G.; Wu, J.; Wang, M.; Niklas, J.; Zhou, H.; Liu, C.; Nitrogen-Defective Polymeric Carbon Nitride Nanolayer Enabled Efficient Electrocatalytic Nitrogen Reduction with High Faradaic Efficiency. *Nano Lett.*, **2020**, 20, 2879-2885.
16. Shipman, M. A.; Symes, M. D.; Recent progress towards the electrosynthesis of ammonia from sustainable resources. *Catal. Today*, **2017**, 286, 57-68.
17. Zhu, S.; Mou, S.; Peng, Q.; Liu, Q.; Luo, Y.; Chen, G.; Gao, S.; Sun X.; Aqueous electrocatalytic N_2 reduction for ambient NH_3 synthesis: recent advances in catalyst development and performance improvement. *J. Mater. Chem. A*, **2020**, 8, 1545-1556.
18. Gao, S.; Zhu, Y.; Chen, Y.; Tian, M.; Yang, Y.; Jiang, T.; Wang, Z. L.; Self-power electroreduction of N_2 into NH_3 by 3D printed triboelectric nanogenerators. *Mater. Today*, **2019**, 28, 17-24.
19. Hollevoet, L.; De Ras, M.; Roeffaers, M.; Hofkens, J.; Martens, J. A.; Energy-Efficient Ammonia Production from Air and Water Using Electrocatalysts with Limited Faradaic Efficiency. *ACS Energy Lett.*, **2020**, 5, 1124-1127.
20. Yao, Y.; Feng, Q.; Zhu, S.; Li, J.; Yao, Y.; Wang, Y.; Wang, Q.; Gu, M.; Wang, H.; Li, H. et al., Chromium Oxynitride Electrocatalysts for Electrochemical Synthesis of Ammonia Under Ambient Conditions. *Small Methods*, **2018**, 3, 1800324.
21. Palys, M. J.; McCormick, A.; Cussler, E. L.; Daoutidis, P.; Modeling and Optimal Design of Absorbent Enhanced Ammonia Synthesis. *Processes*, **2018**, 6, 91.
22. Han, Z.; Choi, C.; Hong, S.; Wu, T.; Soo, Y-L.; Jung, Y.; Qiu, J.; Sun, Z.; Activated TiO_2 with tuned vacancy for efficient electrochemical nitrogen reduction. *Appl. Catal. B. Environ.*, **2019**, 257, 117896.
23. Wang, J.; Yu, L.; Hu, L.; Chen, G.; Xin, H.L.; Feng, X.F.; Ambient ammonia synthesis via palladium-catalyzed electrohydrogenation of dinitrogen at low overpotential. *Nat. Commun.*, **2018**, 9, 1795.

24. Geng, C.; Li, J.; Weiske, T.; Schwarz, H. Complete cleavage of the N≡N triple bond by Ta_2N^+ via degenerate ligand exchange at ambient temperature: A perfect catalytic cycle. *Proc. Natl. Acad. Sci.*, **2019**, 116, 21416-21420.
25. Tang, X.; Hou, Y.; Ng, C. Y.; Ruscic, B.; Pulsed field-ionization photoelectron-photoion coincidence study of the process $N_2 + h\nu \rightarrow N^+ + N + e^-$: Bond dissociation energies of N_2 and N_2^+. *J. Chem. Phys.*, **2005**, 123, 074330.
26. Qin, Q.; Oschatz, M.; Overcoming Chemical Inertness under Ambient Conditions: A Critical View on Recent Developments in Ammonia Synthesis via Electrochemical N_2 Reduction by Asking Five Questions. *ChemElectroChem*, **2020**, **7**, 878-889.
27. Zhao, X.; Hu, G.; Chen, G-F.; Zhang, H.; Zhang, S.; Wang, H.; Comprehensive Understanding of the Thriving Ambient Electrochemical Nitrogen Reduction Reaction. *Adv. Mater.*, **2021**, 33, 2007650.
28. Yang, X.; Nash, J.; Anibal, J.; Dunwell, M.; Kattel, S.; Stavitski, E.; Attenkofer, K.; Chen, J. G.; Yan, Y.; Xu, B.; Mechanistic Insights into Electrochemical Nitrogen Reduction Reaction on Vanadium Nitride Nanoparticles. *J. Am. Chem. Soc.,* **2018**, 140, 41, 13387–13391.
29. Zheng, S.; Li, S.; Mei, Z.; Hu, Z.; Chu, M.; Liu, J.; Chen, X.; Pan, F.; Electrochemical Nitrogen Reduction Reaction Performance of Single-Boron Catalysts Tuned by MXene Substrates. *J. Phys. Chem. Lett.,* **2019**, 10, 22, 6984–6989.
30. Abghoui, Y.; Skulason, E.; Onset potentials for different reaction mechanisms of nitrogen activation to ammonia on transition metal nitride electro-catalysts. *Catal. Today*, **2017**, 286, 69-77.
31. Wang, J.; Yu, L.; Hu, L.; Chen, G.; Xin, H.L.; Feng, X.F.; Ambient ammonia synthesis via palladium-catalyzed electrohydrogenation of dinitrogen at low overpotential. *Nat. Commun.*, **2018**, 9, 1795.
32. Cui, X.; Tang, C.; Zhang, Q.; A Review of Electrocatalytic Reduction of Dinitrogen to Ammonia under Ambient Conditions. *Adv. Energy Mater.*, **2018**, 8, 1800369.
33. Shi, M-M.; Bao, D.; Wulan, B. R.; Li, Y. H.; Zhang, Y. F.; Yan, J. M.; Jiang, Q.; Au Sub-Nanoclusters on TiO_2 toward Highly Efficient and Selective Electrocatalyst for N_2 Conversion to NH_3 at Ambient Conditions. A*dv. Mater.,* **2017**, 29, 1606550.

34. Kordali, V.; Kyriacou, G.; Lambrou, Ch.; Electrochemical synthesis of ammonia at atmospheric pressure and low temperature in a solid polymer electrolyte cell. *Chem. Commun.* **2000**, 1673−1674.

35. Imamura, K.; Kubota, J.; Electrochemical membrane cell for NH_3 synthesis from N_2 and H_2O by electrolysis at 200 to 250 °C using a Ru catalyst, hydrogen-permeable Pd membrane and phosphate-based electrolyte. *Sustain. Energy Fuels* **2018**, 2, 1278−1286.

36. Liu, H-M.; Han, S-H.; Zhao, Y.; Zhu, Y-Y.; Tian, X-L.; Zeng, J-H.; Jiang, J-X.; Xia, B. Y.; Chen, Y.; Surfactant-free atomically ultrathin rhodium nanosheet nanoassemblies for efficient nitrogen electroreduction. *J. Mater. Chem. A*, **2018**, 6, 3211−3217.

37. Kugler, K.; Luhn, M.; Schramm, J. A.; Rahimi, K.; Wessling, M.; Galvanic deposition of Rh and Ru on randomly structured Ti felts for the electrochemical NH_3 synthesis. *Phys. Chem. Chem. Phys.,* **2015**, 17, 3768−3782.

38. Manjunatha, R.; Schechter, A.; Electrochemical synthesis of ammonia using ruthenium–platinum alloy at ambient pressure and low temperature. *Electrochem. Commu.*, **2018**, 90, 96−100.

39. Li, S-J.; Bao, D.; Shi, M-M.; Wulan, B-R.; Yan, J-M.; Jiang, Q.; Amorphizing of Au Nanoparticles by CeO_x –RGO Hybrid Support towards Highly Efficient Electrocatalyst for N_2 Reduction under Ambient Conditions *Adv. Mater.*, **2017**, 29, 1700001.

40. Guo, X.; Yi, W.; Qu, F.; Lu, L.; New insights into mechanisms on electrochemical N_2 reduction reaction driven by efficient zero-valence Cu nanoparticles. *J. Power Sources*, **2020**, 448, 227417.

41. Lin, Y-X.; Zhang, S-N.; Xue, Z. H.; Zhang, J. J.; Su, H.; Zhao, T-J.; Zhai, G-Y.; Li, X-H.; Antonietti, M.; Chen, J-S.; Boosting selective nitrogen reduction to ammonia on electron-deficient copper nanoparticles *Nat. Commun.,* **2019**, 10, 4380.

42. Zhang, X.; Kong, R-M.; Du, H.; Xia, L.; Qu, F.; Highly efficient electrochemical ammonia synthesis via nitrogen reduction reactions on a VN nanowire array under ambient conditions. *Chem. Commun.,* **2018**, 54, 5323−5325.

43. Zhao, X.; Yin, F.; Liu, N.; Li, G.; Fan, T.; Chen, B.; Highly efficient metal–organic-framework catalysts for electrochemical synthesis of ammonia from N_2 (air) and water at low temperature and ambient pressure. *J. Mater. Sci.,* **2017**, 52, 10175−10185.

44. Yang, D. S.; Chen, T.; Wang, Z.; Electrochemical reduction of aqueous nitrogen (N_2) at a low overpotential on (110)-oriented Mo nanofilm. *J. Mater. Chem. A,* **2017**, 5, 18967−18971.
45. Gu, W.; Guo, Y.; Li, Q.; Tian, Y.; Chu, K.; Lithium Iron Oxide (LiFeO2) for Electroreduction of Dinitrogen to Ammonia. *ACS Appl Mater Interfaces,* **2020**, 12, 37258-37264.
46. Fang, W.; Zhao, J.; Wu, T.; Huang, Y.; Yang, L.; Liu, C.; Zhang, Q.; Huang, K.; Yan, Q.; Hydrophilic engineering of VOx-based nanosheets for ambient electrochemical ammonia synthesis at neutral Ph. *J Mater Chem A,* **2020**, 8, 5913- 5918.
47. Xiao, L., Zhu, S., Liang, Y., Li, Z., Wu, S., Luo, S., Chang, C., Zhenduo C.; Nanoporous Nickel–Molybdenum Oxide with an Oxygen Vacancy for Electrocatalytic Nitrogen Fixation under Ambient Conditions. *ACS Appl. Mater. Interfaces*, **2021**, 13, 30722−30730.
48. Kong, Y.; Kong, H.; Lv, C.; and Chen, G.; Engineering Reductive Iron on a Layered Double Hydroxide Electrocatalyst for Facilitating Nitrogen Reduction Reaction. *Adv. Mater. Interfaces*, **2022**, 9, 2102242.
49. Zhao, Y.; Zheng, L.; Shi, R.; Zhang, S.; Bian, X.; Wu, F.; Cao, X.; Waterhouse, G. I. N.; Zhang, T.; Alkali Etching of Layered Double Hydroxide Nanosheets for Enhanced Photocatalytic N_2 Reduction to NH_3 *Adv. Energy Mater.,* **2020**, 10, 2002199.
50. Zhang, S.; Zhao, Y.; Shi, R.; Zhou, C.; Waterhouse, G. I. N.; Wu, L-Z.; Tung, C-H.; Zhang, T.; Efficient Photocatalytic Nitrogen Fixation over $Cu^{\delta+}$-Modified Defective ZnAl-Layered Double Hydroxide Nanosheets. *Adv. Energy Mater.,* **2020**, 10, 1901973.
51. Lv X-W.; Liu Y.; Wang Y. S.; Liu X. L.; Yuan Z-Y.; Encapsulating vanadium nitride nanodots into N,S-codoped graphitized carbon for synergistic electrocatalytic nitrogen reduction and aqueous Zn-N_2 battery. *Appl Catal. B Environ*., **2021**, 280, 119434.
52. Jin, H.; Li, L.; Liu, X.; Tang, C.; Xu, W.; Chen, S.; Song, L.; Zheng, Y.; Nitrogen Vacancies on 2D Layered W_2N_3: A Stable and Efficient Active Site for Nitrogen Reduction Reaction. *Adv. Mater.,* **2019**, 31, 1902709.
53. Matanovic, I.; Garzon, F, H.; Nitrogen electroreduction and hydrogen evolution on cubic molybdenum carbide: a density functional study. *Phys. Chem. Chem. Phys.*, **2018**, 20, 14679-14687.

54. Cheng, H.; Ding, L-X.; Chen, G-F.; Zhang, L.; Xue, J.; Wang, H.; Molybdenum Carbide Nanodots Enable Efficient Electrocatalytic Nitrogen Fixation under Ambient Conditions. *Adv. Mater.,* **2018**, 30, 1803694.
55. Tian, D.; Denny, S. R.; Li, K.; Wang, H.; Kattel, S.; Chen, J. G.; Density functional theory studies of transition metal carbides and nitrides as electrocatalysts. *Chem. Soc. Rev.*, **2021**, 50, 12338.
56. Kong, J.; Kim, M-S.; Akbar, R.; Park, H. Y.; Jang, J. H.; Kim, H.; Hur, K.; Park, H. S.; Electrochemical Nitrogen Reduction Kinetics on a Copper Sulfide Catalyst for NH_3 Synthesis at Low Temperature and Atmospheric Pressure. *ACS Appl. Mater. Interfaces*, **2021**, 13, 24593–24603.
57. Xu, X.; Tian, X.; Sun, B.; Liang, Z.; Cui, H.; Tian, J.; Shao, M.; 1 T-phase molybdenum sulfide nanodots enable efficient electrocatalytic nitrogen fixation under ambient conditions. *Appl. Catal.*, **2020**, 272, 118984.
58. Duan, J.; Shao, D.; Wang, W.; Zhang, D.; Li, C.; Strongly coupled molybdenum phosphide@phosphorus-doped porous carbon derived from MOF used in N_2 electroreduction under ambient conditions. *Micropor. Mesopor. Mater.*, **2021**, 313, 110852.
59. Jiang, X.; He, M.; Tang, M.; Zheng, Q.; Xu, C.; Lin, D.; Nanostructured bimetallic Ni-Fe phosphide nanoplates as an electrocatalyst for efficient N_2 fixation under ambient conditions. *J Mater. Sci.*, **2020**, 55, 15252- 15262.
60. Wang, X.; Feng, Z.; Xiao, B.; Zhao, J.; Ma, H.; Tian, Y.; Pang, H.; Tan, L.; Polyoxometalate-based metal–organic framework-derived bimetallic hybrid materials for upgraded electrochemical reduction of nitrogen. *Green Chem.*, **2020**, 22, 6157-6169.
61. Fu, Y.; Li, K.; Batmunkh, M.; Yu, H.; Donne, S.; Jia, B.; Ma, T.; Unsaturated p-Metal-Based Metal–Organic Frameworks for Selective Nitrogen Reduction under Ambient Conditions. *ACS Appl. Mater. Interfaces*, **2020**, 12, 40, 44830–44839.
62. Zhang, R.; Jiao, L.; Yang, W.; Wand, G.; Jiang, H-L.; Single-atom catalysts templated by metal–organic frameworks for electrochemical nitrogen reduction. *J. Mater. Chem. A*, **2019**, 7, 26371-26377.
63. Zheng, X.; Liu, Y.; Yan, Y.; Li, X.; Yao, Y.; Modulation effect in adjacent dual metal single atom catalysts for electrochemical nitrogen reduction reaction. *Chin. Chem. Lett.*, **2022**, 33, 1455-1458.

64. Balogun, M-S.; Huang, Y.; Qiu, W.; Yang, H.; Ji, H.; Tong, Y.; Updates on the development of nanostructured transition metal nitrides for electrochemical energy storage and water splitting. *Mater. Today*, **2017**, 20, 425-451.

65. Zhong, Y.; Xia, X.; Shi, F.; Zhan, J.; Tu, J.; Fan, H.J.; Transition Metal Carbides and Nitrides in Energy Storage and Conversion. *Adv. Sci.*, **2016**, 3, 1500286.

66. Idrees, M.; Mukhtar, A.; Tehman, A.; Abbas, S. M.; Zhang, Q.; Li, X.; Transition metal nitride electrodes as future energy storage devices: A review. *Mater. Today Commun.,* **2021**, 27, 102363.

67. Cheng, Z.; Qi, W.; Pang, C. H.; Thomas, T.; Wu, T.; Liu, S.; Yang, M.; Recent Advances in Transition Metal Nitride-Based Materials for Photocatalytic Applications. *Adv. Funct. Mater.*, **2021**, 31, 2100553.

68. Abghoui, Y.; Garden, A. L.; Howalt, J. G.; Vegge, T.; Skulason, E.; Electroreduction of N_2 to Ammonia at Ambient Conditions on Mononitrides of Zr, Nb, Cr, and V: A DFT Guide for Experiments. *ACS Catal.*, **2016**, 6, 2, 635–646.

69. Ologunagba, D.; Kattel, S.; Transition metal oxynitride catalysts for electrochemical reduction of nitrogen to ammonia. *Adv. Mater.*, **2021**, 2, 1263-1270.

70. Kohn,W.; Sham L. J.; Self-Consistent Equations Including Exchange and Correlation Effects. *Phys. Rev.*, **1965**, 140, A1133.

71. Kresse, G.; Furthmüller, J.; Efficiency of ab-initio total energy calculations for metals and semiconductors using a plane-wave basis set. *Comput. Mater. Sci.*, **1996**, 6, 15–50.

72. Kresse, G.; Hafner, J.; Ab initio molecular dynamics for open-shell transition metals. *Phys. Rev. B*, **1993**, 48, 13115–13118.

73. Blöchl, P. E.; Projector augmented-wave method. *Phys. Rev. B*, 1994, **50**, 17953–17979.

74. Perdew, J. P.; Wang, Y.; Pair-distribution function and its coupling-constant average for the spin-polarized electron gas. *Phys. Rev. B*, **1992**, 46, 12947–12954.

75. Pack ,J. D.; Monkhorst, H. J.; "Special points for Brillouin-zone integrations"—a reply. *Phys. Rev. B*, **1977**, 16, 1748–1749.

76. Nørskov, J. K.; Rossmeisl, J.; Logadottir, A.; Lindqvist, L.; Kitchin, J. R.; Bligaard, T.; Jónsson, H.; Origin of the Overpotential for Oxygen Reduction at a Fuel-Cell Cathode. *J. Phys. Chem. B*, **2004**, 108, 17886–17892.

77. Norskov, J. K.; Bligaard, T.; Logadottir, A.; Kitchin, J. R.; Chen, J. G.; Pandelov, S.; Stimmung, U.; Trends in the exchange current for hydrogen evolution. *J. Electrochem. Soc.*, **2005**, 152, J23-J26.

78. Li, F.; Tang, Q. First-Principles Calculations of TiB MBeneMonolayers for Hydrogen Evolution. *ACS Appl. Nano Mater.,* **2019**, 2, 7220−7229.

79. Elnabawy, A. O.; Schumann, J.; Bothra, P.; Cao, A.; Norskov, J. K.; The Challenge of CO Hydrogenation to Methanol: Fundamental Limitations Imposed by Linear Scaling Relations. *Top. Catal.*, **2020**, 63, 635–648.

80. Jaf, Z. N.; Altarawneh, M.; Miran, H. A.; Jiang, Z-T.; Geometries, electronic properties and stability of molybdenum and tungsten nitrides low-index surfaces. *Mater. Res. Express*, **2018**, 5, 126402.

81. Wei, Z.; Feng, Y.; Ma, J.; Co-doped graphene edge for enhanced N_2-to-NH_3 conversion. *J. Energy Chem.*, **2020**, 48, 322–327.

82. Yang, X.; Kattel, S.; Nash, J.; Chang, X.; Lee, J. H.; Yan, Y.; Chen, J. G.; Xu, B.; Quantification of Active Sites and Elucidation of the Reaction Mechanism of the Electrochemical Nitrogen Reduction Reaction on Vanadium Nitride. *Angew. Chem. Int. Ed.*, **2019**, 58 , 13768 —13772.

83. Abghoui, Y.; Skúlason, E.; Electrochemical synthesis of ammonia via Mars-van Krevelen mechanism on the (111) facets of group III–VII transition metal mononitrides. *Catal. Today*, **2017**, 286, 78-84.

84. Howalt, J. G.; Vegge, T.; Electrochemical ammonia production on molybdenum nitride nanoclusters. *Phys. Chem. Chem. Phys*., **2013**, 15, 20957-20965.

85. Zeinalipour-Yazdi, C. D.; Hargreaves, J. S. J.; Catlow, C. R. A.; Nitrogen Activation in a Mars–van Krevelen Mechanism for Ammonia Synthesis on Co_3Mo_3N. *J. Phys. Chem.* C, **2015**, 119, 51, 28368–28376.

86. Skúlason, E.; Bligaard, T.; Gudmundsdóttir, S.; Studt, F.; Rossmeisl, J.; Abild-Pedersen, F. Vegge, T.; Jónssonac, H.; Nørskov, J. K.; A theoretical evaluation of possible transition metal electro-catalysts for N_2 reduction. *Phys. Chem. Chem. Phys.,* **2012**,14, 1235-1245.

87. Ai, C.; Vegge, T.; Hansen, H. A.; Metal-Doped PdH(111) Catalysts for CO_2 Reduction. *ChemSusChem,* **2022**, 15, e202200008.

88. Hansen, H. A.; Varley, J. B.; Peterson, A. A.; Norskov, J. K.; Understanding Trends in the Electrocatalytic Activity of Metals and Enzymes for CO_2 Reduction to CO. *J. Phys. Chem. Lett.*, **2013**, 4, 3, 388–392.

Table of Content (TOC) Image